

Gate-tunable crossover between vortex-interaction and pinning dominated regimes in Josephson-coupled lead islands on graphene

Suraina Gupta , Santu Prasad Jana , Rukshana Pervin, and Anjan K. Gupta *

Department of Physics, Indian Institute of Technology Kanpur, Kanpur 208016, India



(Received 28 December 2023; revised 9 May 2024; accepted 1 July 2024; published 12 July 2024)

The resistance of a Josephson junction array consisting of randomly distributed lead islands on exfoliated single-layer graphene shows a broad superconducting transition to zero with an onset temperature close to the transition temperature of bulk Pb. The transition region evolves with the back-gate voltage with two peaks in the temperature derivative of the resistance. The region above the lower-temperature peak is found to be well described by the Berezinskii-Kosterlitz-Thouless model of the thermal unbinding of vortex-antivortex pairs, while that below this peak fits well with the Ambegaokar-Halperin model of thermally activated phase slip or vortex depinning. Thus, a gate-tunable crossover between interaction and pinning dominated vortices is inferred. This is elaborated in terms of free vortices as well as strong pinning sites in this highly inhomogeneous Josephson junction array.

DOI: [10.1103/PhysRevB.110.024506](https://doi.org/10.1103/PhysRevB.110.024506)

I. INTRODUCTION

Superconductivity in two dimensions is intriguing for many reasons, including the abundance of low-energy fluctuations due to the absence of long-range order in two dimensions at finite temperatures [1,2], the presence of a superconductor to insulator transition (SIT) [3–6], and a superinsulator phase [7]. Granularity plays an important role in two-dimensional (2D) superconductors (SCs), and the interplay between Coulomb energy E_C , Josephson coupling energy E_J , and the thermal energy $k_B T$ broadly dictates different regimes. The Coulomb energy E_C is the energy cost of exchanging a Cooper pair with a SC island [8], while E_J dictates the energy cost for two SC grains to have unequal phases. The dominance of E_C leads to a superinsulator phase with localized Cooper pairs and mobile vortices. Competition between E_C and E_J , with both dominating over $k_B T$, leads to SIT, while the dominance of E_J leads to superconductivity.

For $E_J \gg E_C$, the low-energy phase fluctuations manifest as vortex-antivortex pairs at finite temperatures. This broadens the superconducting transition in a 2D SC, and it has mostly been described by the much celebrated works of Berezinskii [9] and Kosterlitz and Thouless [10] and is known as the BKT model. In this model the thermal unbinding of such pairs lead to a finite resistance at any nonzero current below the bulk superconducting critical temperature T_C and above a phase-transition temperature denoted T_{BKT} .

Compared to a three-dimensional SC, the screening capability of currents in a 2D SC for perpendicular magnetic fields is much weaker [11], and so the effective screening length λ_{\perp} , which dictates the intervortex interaction, can exceed the sample size. The logarithmic dependence of the interaction energy on the intervortex separation, required for the BKT

model, is possible only for sample sizes below λ_{\perp} . This imposed finite sample size rules out a true BKT phase transition in thermodynamically large 2D samples, and some dissipation may persist due to finite size induced free vortices below T_{BKT} . Nevertheless, in certain regimes signatures of the BKT transition have been observed [12–14].

Another regime of interest in a finite size 2D array of Josephson junctions (JJs) is described by the Ambegaokar-Halperin (AH) model of thermally activated phase slips (TAPSS) [15,16]. In this case, the vortices drift under a bias current through the intergrain regions and over a potential landscape [17] with vortex pinning sites, dictated by E_J and grain distribution, leading to finite resistance. The smaller E_J regions, finite sample size, and applied bias current in this nonuniform JJ array can contribute free vortices below the overall T_{BKT} [18].

Graphene's exposed two-dimensional electron gas with easy control of its carrier density through a back gate makes it a popular tunable substrate for studying gate-tunable SCs. Superconducting materials that do not wet the graphene surface are ideal for this because one can easily get a 2D array of JJs by using suitable deposition conditions. Many interesting phenomena, including the gate-tunable SIT [3] and magnetic-field-tuned superconductor-metal transition with double quantum criticality [13], have been observed in such SC-graphene hybrid systems. Such samples fall in a regime dominated by the interplay of E_C and E_J , with both being much larger than $k_B T$.

In this paper, we report on the resistance vs temperature $R(T)$ and current-voltage characteristics (IVCs) of a four-probe device consisting of lead islands on exfoliated single-layer graphene, with the back-gate voltage providing a handle on E_J . This work focuses on a regime where the E_J and $k_B T$ interplay dictates the superconducting transition, with E_C being much smaller. The resistance shows a broad gate dependent transition to zero resistance with two peaks in

*Contact author: anjankg@iitk.ac.in

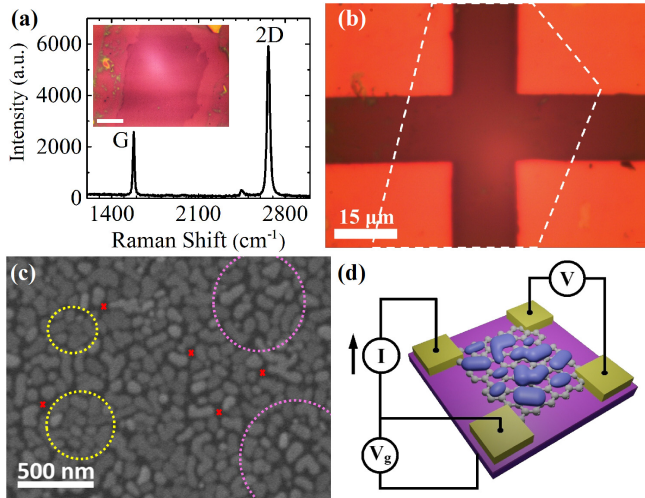


FIG. 1. (a) Raman spectrum taken on graphene showing the two characteristic Raman peaks at approximately 1577 cm^{-1} (G peak) and 2665 cm^{-1} ($2D$ peak). The ratio $I(2D)/I(G) = 2.3$ confirms the graphene is single layer. The inset is the optical image of single-layer graphene, where the white scale bar is $15 \mu\text{m}$. (b) Optical image showing the four contact pads in a van der Pauw geometry. The white dashed line marks the graphene boundary. (c) SEM image showing the distribution of Pb islands (gray) on graphene (black background). The red crosses mark potential sites for strong pinning of vortices, while the pink circles on the right side and yellow ones on the left side outline some low- and high- E_J regions, respectively. (d) Schematic diagram of the four-terminal configuration for electrical measurements in the Pb-graphene hybrid device.

its temperature derivative. The gate voltage dependent $R(T)$ is well described by the BKT and AH models for temperatures above and below the low-temperature peak, respectively. The IVCs in the low-temperature region show a critical current and are found to be consistent with the AH model. Finally, a gate-tunable crossover between interaction and pinning dominated vortex regimes is concluded.

II. EXPERIMENTAL DETAILS

Monolayer graphene was prepared by exfoliating Kish graphite on a highly p -doped silicon wafer with 300 nm thick gate-quality oxide on it. The substrate was first cleaned by sonicating it in acetone, isopropyl alcohol, and deionized water consecutively for 5 min each and then in 50 W oxygen plasma for 2 min [19]. Exfoliation was done within 30 min of this cleaning process. Graphene flakes were then identified under optical microscope. The inset in Fig. 1(a) shows the graphene monolayer used for fabricating the actual device. The Raman spectrum of the graphene flake in Fig. 1(a) gives the ratio of the characteristic G and $2D$ bands as $I(2D)/I(G) = 2.3$, which confirms it is single layer. The absence of the D peak implies graphene is defect-free.

Lithography with resists and wet chemicals was avoided for making electrical contacts on graphene to prevent contamination, which is found to significantly affect the Pb morphology and the graphene-Pb interface transparency. The contacts on the single-layer graphene were made by depositing Cr/Au (5/45 nm) in a van der Pauw geometry using a mechanical mask, as shown in Fig. 1(b). Pb was then

deposited using a thermal evaporation technique. It can be observed from the scanning electron microscope (SEM) image in Fig. 1(c) that Pb formed discrete nanometer-sized islands on graphene in the size range from 30 to 300 nm instead of forming a uniform layer due to its poor wettability on graphene [20,21]. Thus, the Pb-graphene hybrid device is a 2D random array of Josephson junctions with a distribution in island size, shape, and interisland separation. One can also see regions in Fig. 1(c) with the interisland separation larger and smaller than average. One should also note the distribution in the local coordination of islands that occasionally leads to voids surrounded by several islands.

When Pb is deposited on graphene, the substrate temperature during deposition, Pb deposition rate and thickness play a key role in deciding the size, the size distribution of Pb islands, and also their separation [22,23]. Thirty nanometers of Pb were thermally evaporated on graphene by keeping the temperature of the substrate at 71°C . Pb deposited on the SiO_2 substrate surrounding graphene also formed distinct islands with an interisland separation larger than that on graphene, thus preventing any electrical conduction through them. Hence, the electrical conduction happens only through Pb islands that are coupled through graphene. A good-quality interface between Pb and graphene was also ensured by depositing Pb at the high rate of 20 \AA/s , apart from avoiding the wet chemical processes.

After Pb was deposited, devices were promptly mounted on a cryostat which was then cooled in a closed cycle refrigerator to its base temperature of 1.3 K. Low-pass $R - C$ filters with a 15 kHz cutoff frequency as well as high-frequency-cutoff pi filters were installed in the measurement lines at room temperature to minimize electromagnetic noise. The transport measurement wires also go through Cu-powder filters at the base temperature to further reduce the noise interference. The four-probe transport measurements were carried out using a dc-current source as depicted in Fig. 1(d). Current was varied over a limited range, from -20 to $20 \mu\text{A}$, to minimize Joule heating. For the resistance measurements, the device was biased with $1 \mu\text{A}$ current of both polarities. The voltage measured from the device was amplified using a Femto voltage amplifier. Gate voltage V_g between -90 and 90 V was applied to the Si substrate with $10 \text{ k}\Omega$ series resistance. All the measurements reported here were carried out in zero applied magnetic field.

III. THEORETICAL BACKGROUND

In 2D samples with superconducting islands on graphene [3,24], V_g controls the graphene's carrier density, which dictates the interisland Josephson coupling. This results in a V_g dependent E_J . As discussed later, the superconducting transition region in the above sample is best described by the BKT and AH models. The BKT model's applicability was extended from superconducting thin films [12] to 2D arrays of JJs by Lobb *et al.* [2,25]. The AH model of phase slip in a single JJ [15] has been used to understand the flux pinning and creep in granular superconductors, similar to JJ arrays [16,26]. In this section we discuss the details of the BKT and AH models and the role of inhomogeneities and finite sample size that are relevant to this work.

A. Berezinskii-Kosterlitz-Thouless model

The BKT transition is described for ordered 2D thermodynamic systems with interaction between two vortices having a logarithmic dependence on their separation. According to the BKT model, thermal unbinding of the bound vortex-antivortex pairs into free vortices happens above T_{BKT} . A current small enough not to induce vortex unbinding in a 2D SC induces motion of the free vortices due to a Lorentz force in a direction perpendicular to the current. The motion of the free vortices leads to a voltage and thus dissipation. An important length scale in the BKT model is the vortex correlation length $\xi_+(T)$. For $T > T_{\text{BKT}}$, $\xi_+(T) \propto \exp\{b\sqrt{(T_{\text{CO}} - T_{\text{BKT}})/(T - T_{\text{BKT}})}\}$ [1,12]. ξ_+ represents the length scale above which vortex pairs begin to unbind, or alternatively, it is the average distance between two free vortices. Thus, the free-vortex density above T_{BKT} goes as $1/\xi_+^2(T)$, which leads to dissipation and resistance. This resistance, due to the motion of free vortices in the small current limit, is given by [1,12]

$$R/R_N = a \exp[-2b\sqrt{(T_{\text{CO}} - T)/(T - T_{\text{BKT}})}]. \quad (1)$$

Here, a and b are nonuniversal constants of the order of unity, R_N is the normal state resistance, and T_{CO} is the critical transition temperature.

The perpendicular screening length [11] in a 2D superconductor is given by $\lambda_\perp = 2\lambda^2/d$, with λ being the penetration depth and d being the thickness. Thus, $\lambda_\perp \gg \lambda$, and it can exceed the size of the 2D SC samples. λ_\perp also dictates the crossover in the separation r dependence of the intervortex interaction force, which varies as $1/r$ for $r < \lambda_\perp$ and as $1/r^2$ for $r > \lambda_\perp$. Thus, the intervortex interaction energy is logarithmic for $r < \lambda_\perp$, and it decays much faster for larger r . The logarithmic interaction is crucial for the applicability of the BKT physics.

The BKT transition temperature T_{BKT} of a uniform JJ array depends on E_J as [27] $T_{\text{BKT}} = \alpha E_J(T_{\text{BKT}})$. Here, α depends on the array configuration, and $E_J(T)$ is the temperature dependent Josephson coupling energy. For a uniform square array $\alpha = \pi/2k_B$, with k_B being the Boltzmann constant. For such a uniform JJ array, λ_\perp is given by [2,28] $\lambda_\perp(T) = \Phi_0/[2\pi\mu_0 i_C(T)]$. Here, i_C is the critical current of each junction, which depends exponentially on temperature [25] for proximity junctions.

In a uniform array of Josephson junctions with lattice parameter a_0 , the energy required to generate a vortex-antivortex pair separated by r is given by [29] $2\pi E_J \ln(r/a_0)$. Thus, there is a finite probability for creation of such pairs with finite separation at nonzero temperatures. The energy required to produce a single vortex, on the other hand, is given by $\pi E_J \ln(\mathcal{L}/a_0)$. Here, $\mathcal{L} \equiv \min[L, \lambda_\perp]$, with L being the array size. Thus, a finite size system or a small λ_\perp can contribute to the formation of free vortices at nonzero temperatures [29]. This results in the free-vortex density [28,29] $n_{\text{fs}}(T) \propto (e\mathcal{L}/a_0)^{-\pi E_J(T)/k_B T}$. For infinite samples, as T_{BKT} is approached from above, ξ_+ grows and diverges at T_{BKT} , leading to no free vortices below T_{BKT} . But for a finite size system, a cutoff is imposed on ξ_+ at a temperature slightly above T_{BKT} because ξ_+ cannot grow beyond [30] \mathcal{L} .

The behavior of ξ_+ is also modified in the presence of a finite applied current due to current induced vortex

pair-breaking effects that are important down to zero temperature. Thus, ξ_+ does not diverge at T_{BKT} for finite currents. The finite current introduces an extrinsic length scale r_C in the system [2,31], such that the vortex pairs with separation more than r_C unbind due to applied current. The density of such current-unbound free vortices for $T < T_{\text{BKT}}$ is given by [28,29] $n_{\text{cu}}(T) \propto [i_C(T)/i]^{-\pi E_J(T)/k_B T}$, with i being the bias current per junction. In summary, unbound or free vortices may be present in a 2D SC JJ array at any nonzero temperature for several reasons, including finite size and current effects. Consequently, the free-vortex density may not abruptly jump to zero with cooling at T_{BKT} , leading to a widening of the transition region.

B. Vortex pinning and the Ambegaokar-Halperin model

The AH theory quantitatively models the small finite resistance observed in an overdamped Josephson junction with a bias current smaller than the critical current. This resistance arises due to the TAPS processes. Defining $x = I/I_C$, with I being the bias current and I_C being the junction critical-current value (in the absence of thermal fluctuations), the time-averaged voltage for the Josephson junction for $x < 1$ at temperature T is given by [15,32]

$$V = 2(I_C R_N) \sqrt{1 - x^2} \exp[-\gamma(\sqrt{1 - x^2} + x \sin^{-1} x)] \times \sinh(\pi \gamma x/2). \quad (2)$$

Here, γ is the ratio of the zero-current barrier height, i.e., $2E_J$, to $k_B T$, and R_N is the normal state resistance. Note that the above expression is valid for large γ values. Furthermore, in the limit [15] $x \rightarrow 0$, the above expression leads to a resistance,

$$R = R_N [I_0(\gamma/2)]^{-2}. \quad (3)$$

Here, I_0 is the modified Bessel function of zeroth order. The detailed IVC in Eq. (2) is nonlinear as the applied current reduces the barrier for phase slip. The barrier vanishes as the bias current approaches the critical current I_C .

In a uniform square 2D Josephson junction array, Rzchowski *et al.* [17] calculated the potential seen by a single vortex to be like an ‘‘egg crate.’’ In this case, the barriers are at the junctions between two superconducting islands, and the minima lie at the junctions of four superconducting islands. On the application of bias current, a vortex existing in this array will move in this potential, crossing the barriers at the junctions by thermal activation and resulting in a phase slip of 2π across the junction it moves through. Tinkham [16] argued that the kinetics of the driven, highly damped, thermally activated processes in granular superconductors involve the same 2π phase slip physics as the thermally activated phase motion in a single, overdamped, current-driven Josephson junction.

For a JJ array, the actual barrier seen by a vortex in a minimum is lower than that in a single junction. For a uniform square JJ array, this barrier is found to be close to [25] $0.2E_J$, while that for a triangular array is [25] $0.043E_J$. For a random array, we can expect a distribution in barrier energies due to the varied island coordination and E_J values. For a granular superconductor consisting of polycrystalline $\text{YBa}_2\text{Cu}_3\text{O}_{7-\delta}$, Bhalla and Pratima [33,34] used the modified expression

$\gamma = A(1 - T/T_{CO})^m$ for the normalized barrier height to explain the dissipation. Here, m is a variable exponent, and the constant A includes an unspecified dependence of γ on the applied magnetic field, with T/T_{CO} being the reduced temperature. Similarly, for our Pb-graphene hybrid system, we modify the zero-bias resistance (3) to

$$R = R_N \{I_0 [A(1 - T/T_{CO})^m / 2]\}^{-2}. \quad (4)$$

Here, both A and m can be expected to depend on the gate voltage V_g .

As discussed earlier, a finite density of free vortices can exist at nonzero temperature below T_{BKT} due to nonzero current bias and finite sample size. An applied bias current drives the free vortices and antivortices towards the opposite edges of the JJ array. In a steady state, the vortices driven out will get replaced by newly generated pairs in the bulk and by those entering from the edges. The free vortices will have to overcome the pinning sites, and we assume the AH model is most appropriate for this depinning physics. As discussed later, strong inhomogeneities and finite size can add to free vortices and the dissipation.

C. Effect of inhomogeneities and finite size

An inhomogeneous JJ array has a distribution in E_J values as well as in the local coordination of islands. This leads to a potential-energy landscape for individual vortices with features at different length scales. The voids, mentioned earlier, lead to sharp local minima as strong pinning sites, while the E_J patches larger and smaller than the average amount to mounds and puddles, respectively. The bias current will give an overall slope, which is opposite for the two vortex polarities, to this landscape perpendicular to the bias current, while the sample edges will have sharp down steps where the vortices can escape. The inhomogeneity in E_J will also lead to an inhomogeneous distribution of the bias current with smaller E_J regions carrying lower current. The intervortex interaction will add complications to this simple independent vortex picture.

The vortex-antivortex pair excitations in shallow regions will occur more because they will cost less energy. Under a bias current some of these vortices can move out into other regions at finite temperature. The depinning will also affect the current induced free-vortex density as the vortex and antivortex of the pair have to overcome pinning sites to get sufficiently separated. In this sense, the AH model will play a role in the creation of free vortices as well as their movement until they exit from an edge.

The inverse of this process, due to finite size, can also contribute to dissipation. A free vortex can enter, preferably through the weaker E_J regions near a sample edge, under a bias current and at finite temperature and occupy a pinning site. Such a vortex will face a barrier predominantly dictated by the local E_J values at the edge to reach a pinning site. The vortex activation over a barrier and depinning play important roles in its creation and further movement into the sample under bias current until it either exits from the opposite edge or it meets an antivortex and gets annihilated.

When the sample is cooled, E_J becomes nonzero at T_{CO} and then increases further with cooling. The pinning will be

ineffective just below T_{CO} and down to certain temperature since the thermal energy $k_B T$ will exceed the E_J dependent pinning energies. The dissipation in this regime can thus be described by the vortex-antivortex interaction physics, i.e., a BKT model with a suitable (or average) temperature dependent E_J . With further cooling, the pinning energy at few sites will start to exceed $k_B T$, and there could be a mixed regime with an interplay between intervortex interaction and pinning. Moreover, the free-vortex density due to inhomogeneities and finite sample size under an applied bias current will start dominating over that expected from the BKT physics of a uniform array. Thus, below a certain temperature the pinning physics will predominantly dictate the dissipation.

IV. RESULTS AND ANALYSIS

A. Gate dependent resistance measurements

Figure 2(a) displays the measured resistance with temperature at $V_g = 0$ V for the graphene-Pb hybrid sample. It shows a broad resistive transition with cooling as the resistance R drops gradually starting from a superconductivity onset temperature of about 7 K, which is close to the superconductivity critical temperature of the bulk lead. The broadened $R(T)$ curve, displaying a two-step transition to the zero-resistance state, is characteristic of granularity in SCs [35–37]. The derivative of the resistance with respect to temperature, i.e., dR/dT [see Fig. 2(b)], exhibits two peaks. The higher-temperature narrow peak corresponds to the onset temperature T_{CO} , which is associated with superconductivity inside the Pb islands. Below T_{CO} , a weak Josephson coupling with energy E_J sets in, leading to weak phase coherence between islands with phase fluctuations proliferating as vortices.

With cooling, E_J increases, and a relatively less steep reduction in resistance, marked by a broader peak in dR/dT compared to that at T_{CO} , is observed. The temperature corresponding to this peak marks a crossover between two regimes, as discussed later, and thus, it is denoted T_X . This peak also has some fine structure, which presumably arises from a distribution in E_J values and is influenced by the detailed island distribution in this finite size sample. As the temperature is further lowered, global phase coherence is achieved, leading to a macroscopic SC state. The temperature T_C^{zero} at which the macroscopic SC state is achieved is defined at 1% of R_{10K} .

There is significant variation in $R(T)$ and the dR/dT curves with V_g , as shown in Figs. 2(c) and 2(d). The carrier density in this graphene, which is electron doped due to the interface traps and the presence of Pb, is the lowest at $V_g = -90$ V, and it increases monotonically with V_g . The Dirac point in this sample is not accessible due to significant electron doping, as seen from the normal state resistance variation with V_g in Fig. 2(f). The Josephson coupling between Pb islands, mediated by graphene, is expected to increase with V_g due to the increase in carrier density in graphene. As a result, when V_g is increased from -90 to $+90$ V, T_C^{zero} increases from about 2 to 4 K, although T_{CO} remains nearly the same as shown in Fig. 2(e). Thus, the transition region between T_{CO}

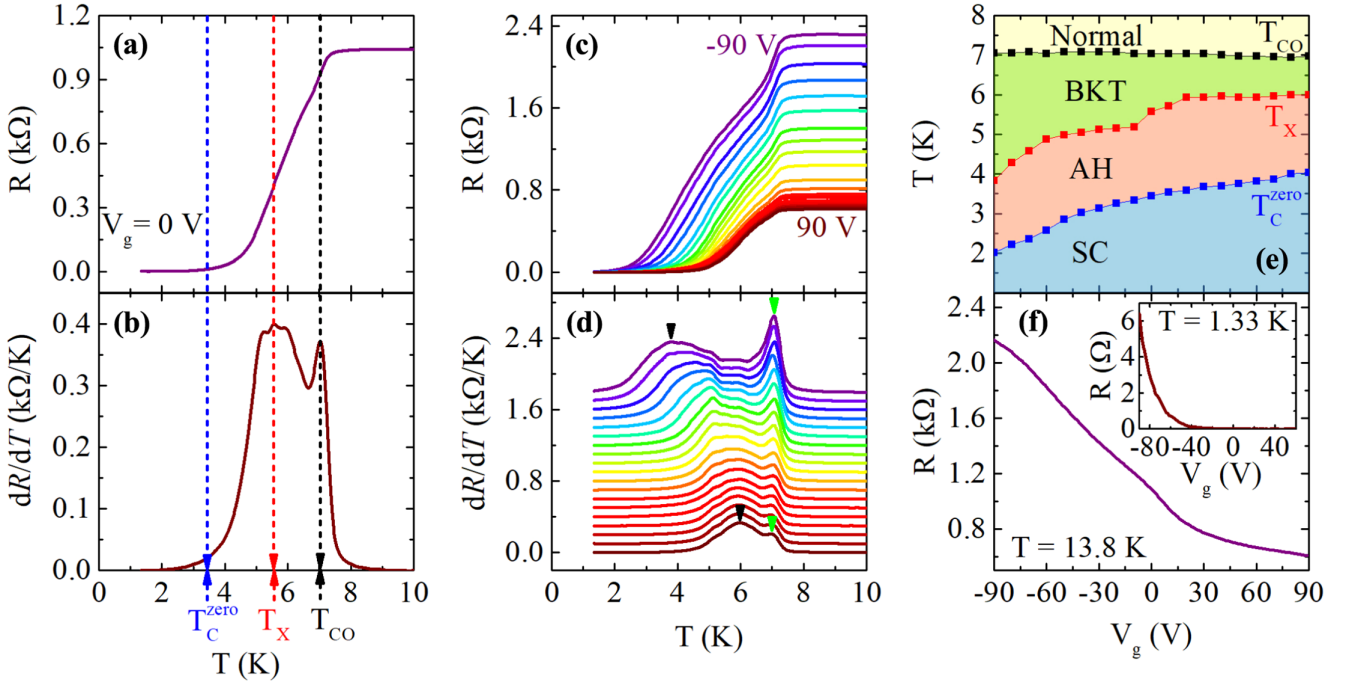


FIG. 2. (a) Four-probe resistance R (at $1 \mu\text{A}$ bias current) and (b) its first derivative dR/dT as a function of temperature at gate voltage $V_g = 0 \text{ V}$, illustrating the two-step resistive transition. The vertical black, red, and blue dashed lines mark the onset temperature $T_{\text{CO}} = 7.04 \text{ K}$, the crossover temperature $T_X = 5.58 \text{ K}$, and the global SC temperature $T_{\text{C}}^{\text{zero}} = 3.44 \text{ K}$, respectively. (c) and (d) The variation in R and dR/dT versus T , respectively, with gate voltage V_g . Here, V_g varies from -90 to 90 V (upper to lower curve) with $\Delta V_g = 10 \text{ V}$. The curves in (d) have been uniformly shifted vertically for clarity, and the arrows indicate the local maxima. (e) The variations of T_{CO} , T_X , and $T_{\text{C}}^{\text{zero}}$ with V_g . (f) The V_g dependence of the resistance at $T = 13.8 \text{ K}$, showing that the Dirac point of the hybrid system is below -90 V . The inset of (f) shows the variation of resistance with V_g and at the 1.33 K base temperature.

and $T_{\text{C}}^{\text{zero}}$ widens with the reduction in V_g as T_X decreases. Interestingly, with decreasing V_g or E_J , the peak in dR/dT at T_{CO} becomes more pronounced, indicating a much sharper onset of superconductivity. At the same time the peak at T_X becomes broader with decreasing V_g , and the fine structure in it becomes clearer.

Figure 3 shows plots of R/R_N versus T/T_{CO} at several V_g values. The green dashed lines are the least-squares fits down to T_X using Eq. (1), yielding a , b , and T_{BKT} as the fitting parameters. R_N is taken to be 90% of the $R_{10\text{K}}$ value at the corresponding V_g . Since the BKT fit works well for $T_{\text{CO}} > T > T_X$, the vortex dynamics in this regime is dominated by logarithmic intervortex interactions. Deviation from Eq. (1) is observed below T_X , which is slightly more than T_{BKT} , as seen in Fig. 3. The system should go to the zero-resistance state below T_{BKT} , but it starts deviating from the BKT fit above T_{BKT} , with a resistance tail implying the presence of free vortices well below T_{BKT} . The latter could arise due to inhomogeneity, current induced unbinding, and finite size effects, as discussed in Sec. III.

As the system cools down, E_J increases, and more Pb islands become phase coherent due to proximity induced superconductivity in graphene [27]. When the pinning energy of some dominant pinning sites exceeds $k_B T$ substantially, a pinning dominated regime may occur. The pinning here does not refer to the intraisland pinning, which would cost significantly more energy. As discussed in Sec. III C, one can have smaller than average E_J patches that contribute free vortices. But with some strong pinning sites, the dissipation

is dominated by pinning. In fact, the free-vortex density may also get affected by the presence of the strong pinning sites. Equation (4) is thus fitted to the resistive tails and below T_X . As discussed earlier, the unspecified V_g dependence of γ is included in A and m . With further cooling, both the free-vortex density and the mobility decreases, and thus, below $T_{\text{C}}^{\text{zero}}$, one gets a zero-resistance state.

Equation (4) breaks down for $T > T_X$, as the intervortex interaction starts dominating over the pinning, leading to the BKT regime. For $T < T_X$, pinning dominates over the intervortex interaction. Fitting parameters from the two models are plotted in Fig. 4 as a function of V_g . It can be observed in Fig. 4(a) that the parameters a and b from Eq. (1) are of the order of unity, as stated in the theory [12]. The monotonic increment of T_{BKT} with an increase in V_g is also consistent with the literature [24,27]. In Fig. 4(b), the fitting parameter A from Eq. (4) increases with V_g . This is expected because Josephson coupling grows with V_g . However, the exponent m decreases slightly with an increase in V_g and then saturates.

B. V - I characteristics

Figures 5(a) and 5(b) show the measured voltage as a function of the bias current in the four-probe configuration at different temperatures for $V_g = -30$ and 30 V , respectively. The nonhysteretic and smooth voltage without any abrupt jump as a function of current suggests that the system is in the overdamped limit with negligible heating effects. Further,

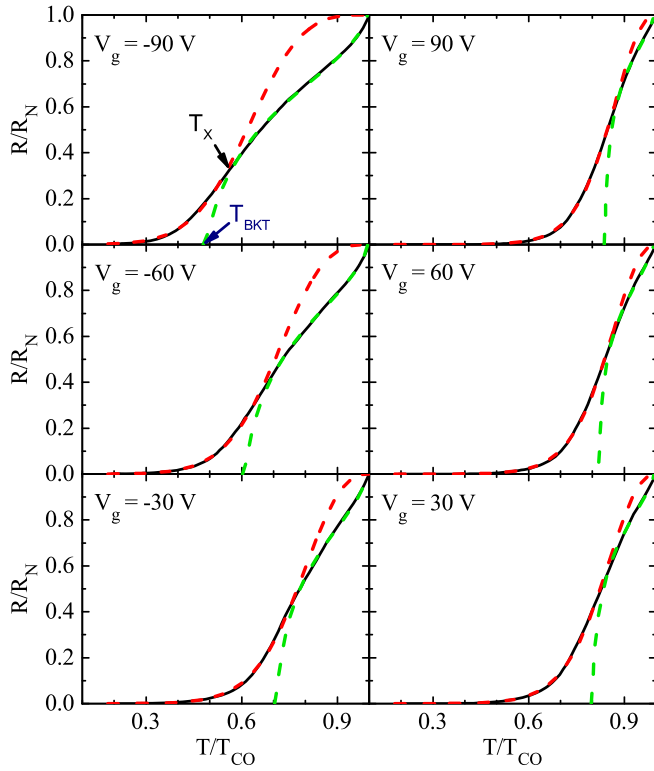


FIG. 3. Normalized resistance as a function of normalized temperature at $V_g = -90, -60, -30, 30, 60,$ and 90 V. The green and red dashed lines are the fits using the BKT equation (1) and the AH equation (4), respectively.

there is a nonzero slope at zero bias current, particularly for temperatures close to T_X , as shown in the zooms in Figs. 5(c) and 5(d). The red dashed curves in these plots are the fits obtained using the Eq. (2) with the fitting parameter γ , as shown in Figs. 5(e) and 5(f) as red squares, as a function of temperature. The solid lines show $\gamma = A(V_g)(1 - T/T_{CO})^m$, with A and m taken from Fig. 4(b) at the respective V_g values that were obtained by fitting Eq. (4) to the experimental $R(T)$ curves. The agreement between the two γ provides significant support for the applicability of the AH model. Further, the decrease of γ with increasing temperature is consistent with the reduction in Josephson coupling with temperature leading to easier flux transport.

Figure 6(a) shows the measured $V(I)$ curves for a wider V_g range at $T = 1.33$ K. The fits with Eq. (2) are made to identify the other fitting parameter I_C , which is plotted

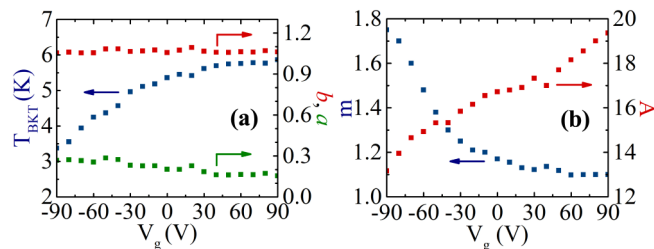


FIG. 4. Fitting parameters (a) a, b , and T_{BKT} for $T > T_X$ and (b) m and A for $T < T_X$, plotted as a function of V_g .

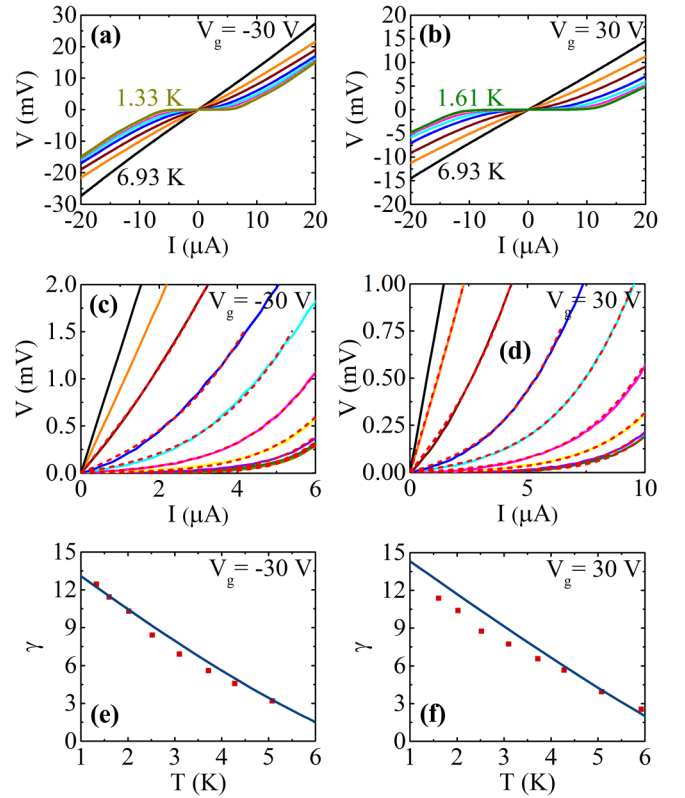


FIG. 5. (a) $V-I$ characteristics at temperatures $T = 1.33, 1.61, 2.02, 2.52, 3.10, 3.72, 4.28, 5.08$ K $< T_X$ and $5.92, 6.93$ K $> T_X$ for $V_g = -30$ V. (b) $V-I$ characteristics at temperatures $T = 1.61, 2.02, 2.52, 3.10, 3.72, 4.28, 5.08, 5.92$ K $< T_X$ and 6.93 K $> T_X$ for $V_g = 30$ V. (c) and (d) Zooms of these curves. Red dashed lines are the fits to Eq. (2) for $V(I)$ curves at $T < T_X$. (e) and (f) Temperature dependence of γ obtained by fitting $V(I)$ (red squares) and that deduced from A and m (blue lines) used in fitting $R(T)$ curves below T_X .

as red squares in Fig. 6(b) as a function of V_g . On the application of bias current, vortices experience Lorentz force, and analogously, there is tilting of the pinning potential transverse to the applied current. When the bias current is increased and it eventually reaches a critical value where the pinning energy barrier diminishes, there is free-flow motion of vortices. We identify this fitted I_C value as the depinning current.

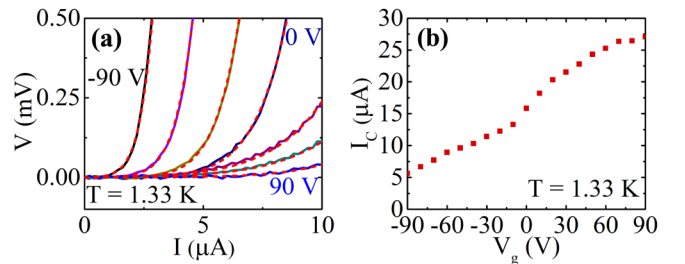


FIG. 6. (a) $V-I$ characteristics for $V_g = -90, -60, -30, 0, 30, 60$ and 90 V at $T = 1.33$ K. The red dashed lines are the fit to Eq. (2). (b) The V_g dependence of I_C obtained from the fits in (a).

V. DISCUSSION AND CONCLUSION

The Appendix estimates some of the relevant quantities for the studied sample at a specific V_g value using the theoretical results for a uniform square array. This shows that λ_{\perp} stays well above the sample size, justifying the applicability of the BKT model. The free-vortex density expected from this approach due to finite size and bias current should drop extremely rapidly at T_{BKT} . This is contrary to the observed dissipation below T_X or T_{BKT} . The I_C values from the AH model fits of the IVCs appear to be reasonable compared to those anticipated from a uniform JJ array.

As discussed before, the nonuniformities in a random JJ array can occur at different length scales, leading to regions of different E_J in addition to the local pinning sites. Thus, one can imagine a somewhat oversimplified picture with a distribution in T_{BKT} with some sort of an overall average T_{BKT} . The small T_{BKT} (or E_J) regions would still contribute free vortices [18] at temperatures below the average T_{BKT} but above their local T_{BKT} . Thus, the pinning can be the actual hindrance in dissipation until the temperature drops below the lowest T_{BKT} of all the regions where the free-vortex density will vanish. The pinning physics, as pointed out earlier, may also contribute to the free-vortex generation process.

It is also noteworthy that the observed crossover between the two regimes at T_X shows a smooth matching at this temperature without any noticeable regime beyond the two models. Further, this is the case for all studied V_g values. Thus, a single model should be able to describe both regimes. The model of Lobb *et al.* [25] combined the AH model and the BKT model, with the former describing the mobility of the free vortices and the latter dictating their density. Eventually, the mobility does not depend so drastically on temperature compared to the free-vortex density in uniform arrays, and thus, the BKT model works in the whole temperature range.

In conclusion, the studied Pb-graphene hybrid system exhibits a gate-tunable two-step transition to the zero-resistance state as it is cooled below T_{CO} , i.e., when the islands become superconducting. The initial dissipation from the motion of the free vortices fits well with the BKT model. But with cooling, the pinning dominates below a crossover temperature T_X . This regime fits well with the AH theory. The E_J inhomogeneities broaden the BKT transition, leading to free vortices over a wide temperature range, and at the same time the pinning sites become much stronger. The increase in T_X with V_g provides a tunability in this crossover. The overall transition width increases with decreasing V_g as T_{CO} remains the same, while T_X , T_{BKT} , and T_C^{zero} decrease. Last, this experiment has enabled us to acquire a deeper understanding of the dissipation in nonuniform JJ arrays.

ACKNOWLEDGMENTS

We thank S. Banerjee and P. Raychaudhuri for discussions. We acknowledge SERB-DST of the Government of India and IIT Kanpur for financial support.

APPENDIX: SOME ESTIMATES USING THE UNIFORM JJ ARRAY RESULTS

Some quantitative estimates are discussed here for $V_g = -30$ V using the theoretical results for a uniform square array and the temperature dependence of the critical current expected for graphene-superconductor Josephson junctions. From the relations [25] $k_B T_{\text{BKT}} = \pi E_J(T_{\text{BKT}})/2$, $E_J = \Phi_0 i_C / (2\pi)$, and $\lambda_{\perp}(T) = \Phi_0 / [2\pi \mu_0 i_C(T)]$, we get $i_C(T_{\text{BKT}})/T_{\text{BKT}} = 26.64$ nA/K and $T_{\text{BKT}} \lambda_{\perp}(T_{\text{BKT}}) = 9.85$ mm K. Using these for $V_g = -30$ V, for which $T_{\text{BKT}} = 5$ K, we get $i_C(T_{\text{BKT}}) = 133.5$ nA and $\lambda_{\perp}(T_{\text{BKT}}) = 1.97$ mm. In the temperature range of our study for such proximity based Josephson junctions [25] we use $i_C(T) = i_C(0)[1 - (T/T_{\text{CO}})]^2$ to find i_C , using $i_C(T_{\text{BKT}})$, at different temperatures. This relation is applicable because the ratio of the interisland separation and the normal metal (graphene) coherence length is much less than 1 and it does not change much over the temperature range of interest here. This gives $i_C = 1.07$ μA at $T = 1.33$ K and thus $\lambda_{\perp}(1.33\text{K}) = 0.25$ mm. The latter exceeds the sample size by more than 1 order of magnitude.

Estimating 150 junctions in a linear size of about 15 μm in our sample, we get the scaled critical current $150i_C = 159$ μA at 1.33 K. It is 20 μA at T_{BKT} . Both are much larger than the 1 μA bias current used in $R(T)$ measurements. The 159 μA current is also much larger than the AH model fit to IVCs, which gives $I_C = 11.6$ μA at 1.33 K [see Fig. 6(b)]. On the other hand, the BKT model does not fit the $R(T)$ and IVCs, while the AH model with a $0.2E_J$ barrier (i.e., the value for the uniform square array [2]) will have $I_C = 15i_C = 15.9$ μA at 1.33 K. This is comparable to the AH fitted value. It is estimated to be $0.022 \times 150i_C = 3.5$ μA for a uniform triangular array.

The free-vortex density, as discussed earlier, due to finite size is given by $n_{\text{fs}} \propto (eL/a_0)^{-\pi E_J(T)/k_B T}$, while that due to finite bias current is $n_{\text{cu}} \propto [i_C(T)/i]^{-\pi E_J(T)/k_B T}$. Both these expressions are for a uniform JJ array. The quantity eL/a_0 is temperature independent, and for the sample studied here, it is about 400, considering $L = 15$ μm and $a_0 = 100$ nm. The quantity $i_C(T)/i$, which is the same as $I_C(T)/I$, is about 150 at 1.33 K for $I = 1$ μA , and it will decrease with increasing temperature. Thus, current-unbound free vortices will dominate if we use uniform square array results. Note that both of these would still amount to a much sharper drop in the free-vortex density with temperature [18] at T_{BKT} than the observed drop in resistance in our system.

- [1] A. M. Kadin, K. Epstein, and A. M. Goldman, Renormalization and the Kosterlitz-Thouless transition in a two-dimensional superconductor, *Phys. Rev. B* **27**, 6691 (1983).
 [2] R. Newrock, C. Lobb, U. Geigenmüller, and M. Octavio, The two-dimensional physics of Josephson-junction arrays, *Solid State Phys.* **54**, 263 (2000).

- [3] A. Allain, Z. Han, and V. Bouchiat, Electrical control of the superconducting-to-insulating transition in graphene-metal hybrids, *Nat. Mater.* **11**, 590 (2012).
 [4] B. Hen, X. Zhang, V. Shelukhin, A. Kapitulnik, and A. Palevski, Superconductor-insulator transition in two-dimensional indium-indium-oxide composite,

- Proc. Natl. Acad. Sci. USA **118**, e2015970118 (2021).
- [5] Y. Li, C. L. Vicente, and J. Yoon, Transport phase diagram for superconducting thin films of tantalum with homogeneous disorder, *Phys. Rev. B* **81**, 020505(R) (2010).
- [6] A. T. Bollinger, G. Dubuis, J. Yoon, D. Pavuna, J. Misewich, and I. Božović, Superconductor–insulator transition in $\text{La}_{2-x}\text{Sr}_x\text{CuO}_4$ at the pair quantum resistance, *Nature (London)* **472**, 458 (2011).
- [7] T. I. Baturina and V. M. Vinokur, Superinsulator–superconductor duality in two dimensions, *Ann. Phys. (NY)* **331**, 236 (2013).
- [8] H. S. J. van der Zant, W. J. Elion, L. J. Geerligs, and J. E. Mooij, Quantum phase transitions in two dimensions: Experiments in Josephson-junction arrays, *Phys. Rev. B* **54**, 10081 (1996).
- [9] V. L. Berezinskii, Destruction of long-range order in one dimensional and two-dimensional systems possessing a continuous symmetry group. II. Quantum systems, *Zh. Eksp. Teor. Fiz.* **61**, 1144 (1971) [*Sov. Phys. JETP* **34**, 610 (1972)].
- [10] J. M. Kosterlitz and D. J. Thouless, Ordering, metastability and phase transitions in two-dimensional systems, *J. Phys. C* **6**, 1181 (1973).
- [11] J. Pearl, Current distribution in superconducting films carrying quantized fluxoids, *Appl. Phys. Lett.* **5**, 65 (1964).
- [12] B. Halperin and D. R. Nelson, Resistive transition in superconducting films, *J. Low. Temp. Phys.* **36**, 599 (1979).
- [13] Y. Sun, H. Xiao, M. Zhang, Z. Xue, Y. Mei, X. Xie, T. Hu, Z. Di, and X. Wang, Double quantum criticality in superconducting tin arrays–graphene hybrid, *Nat. Commun.* **9**, 2159 (2018).
- [14] T. Schneider, A. D. Caviglia, S. Gariglio, N. Reyren, and J.-M. Triscone, Electrostatically-tuned superconductor–metal–insulator quantum transition at the $\text{LaAlO}_3/\text{SrTiO}_3$ interface, *Phys. Rev. B* **79**, 184502 (2009).
- [15] V. Ambegaokar and B. I. Halperin, Voltage due to thermal noise in the dc Josephson effect, *Phys. Rev. Lett.* **22**, 1364 (1969).
- [16] M. Tinkham, Resistive transition of high-temperature superconductors, *Phys. Rev. Lett.* **61**, 1658 (1988).
- [17] M. S. Rzchowski, S. P. Benz, M. Tinkham, and C. J. Lobb, Vortex pinning in Josephson-junction arrays, *Phys. Rev. B* **42**, 2041 (1990).
- [18] L. Benfatto, C. Castellani and T. Giamarchi, Broadening of the Berezinskii–Kosterlitz–Thouless superconducting transition by inhomogeneity and finite-size effects, *Phys. Rev. B* **80**, 214506 (2009).
- [19] Y. Huang, E. Sutter, N. N. Shi, J. Zheng, T. Yang, D. Englund, H. J. Gao, and P. Sutter, Reliable exfoliation of large-area high-quality flakes of graphene and other two-dimensional materials, *ACS Nano* **9**, 10612 (2015).
- [20] X. Han, Y. Wu, H. Xiao, M. Zhang, M. Gao, Y. Liu, J. Wang, T. Hu, X. Xie, and Z. Di, Disorder-induced quantum Griffiths singularity revealed in an artificial 2D superconducting system, *Adv. Science* **7**, 1902849 (2020).
- [21] X. Han, M. Gao, Y. Wu, G. Mu, M. Zhang, Y. Mei, P. K. Chu, X. Xie, T. Hu, and Z. Di, Gate-tunable two-dimensional superconductivity revealed in flexible wafer-scale hybrid structures, *J. Mater. Chem. C* **8**, 14605 (2020).
- [22] X. Yu, P. M. Duxbury, G. Jeffers, and M. A. Dubson, Coalescence and percolation in thin metal films, *Phys. Rev. B* **44**, 13163 (1991).
- [23] X. Liu, Y. Han, J. W. Evans, A. K. Engstfeld, R. J. Behm, M. C. Tringides, M. Hupalo, H. Q. Lin, L. Huang, K. M. Ho, D. Appy, P. A. Thiel, and C. Z. Wang, Growth morphology and properties of metals on graphene, *Prog. Surf. Sci.* **90**, 397 (2015).
- [24] Z. Han, A. Allain, H. Arjmandi-Tash, K. Tikhonov, M. Feigel’man, B. Sacépé, and V. Bouchiat, Collapse of superconductivity in a hybrid tin–graphene Josephson junction array, *Nat. Phys.* **10**, 380 (2014).
- [25] C. J. Lobb, D. W. Abraham, and M. Tinkham, Theoretical interpretation of resistive transition data from arrays of superconducting weak links, *Phys. Rev. B* **27**, 150 (1983).
- [26] R. Gross, P. Chaudhari, D. Dimos, A. Gupta, and G. Koren, Thermally activated phase slippage in high- T_c grain-boundary Josephson junctions, *Phys. Rev. Lett.* **64**, 228 (1990).
- [27] M. V. Feigel’man, M. A. Skvortsov, and K. S. Tikhonov, Proximity-induced superconductivity in graphene, *JETP Lett.* **88**, 747 (2008).
- [28] S. T. Herbert, Y. Jun, R. S. Newrock, C. J. Lobb, K. Ravindran, H. K. Shin, D. B. Mast, and S. Elhamri, Effect of finite size on the Kosterlitz–Thouless transition in two-dimensional arrays of proximity-coupled junctions, *Phys. Rev. B* **57**, 1154 (1998).
- [29] J. Holzer, R. S. Newrock, C. J. Lobb, T. Aouaroun, and S. T. Herbert, Finite-size effects and dynamical scaling in two-dimensional Josephson junction arrays, *Phys. Rev. B* **63**, 184508 (2001).
- [30] T. Schneider and S. Weyeneth, Suppression of the Berezinskii–Kosterlitz–Thouless and quantum phase transitions in two-dimensional superconductors by finite-size effects, *Phys. Rev. B* **90**, 064501 (2014).
- [31] S. W. Pierson, M. Friesen, S. M. Ammirata, J. C. Hunnicutt, and L. A. Gorham, Dynamic scaling for two-dimensional superconductors, Josephson-junction arrays, and superfluids, *Phys. Rev. B* **60**, 1309 (1999).
- [32] A. C. Wright, K. Zhang, and A. Erbil, Dissipation mechanism in a high- T_c granular superconductor: Applicability of a phase-slip model, *Phys. Rev. B* **44**, 863 (1991).
- [33] G. L. Bhalla and Pratima, On the dissipation mechanism in polycrystalline $\text{Ba}_2\text{YCu}_3\text{O}_{7-\delta}$ superconductor, *Phys. C (Amsterdam, Neth.)* **406**, 154 (2004).
- [34] G. L. Bhalla and Pratima, Vortex–antivortex behaviour and thermally activated phase slip in a polycrystalline $\text{YBa}_2\text{Cu}_3\text{O}_{7-\delta}$ superconductor, *Supercond. Sci. Technol.* **20**, 1120 (2007).
- [35] S. Eley, S. Gopalakrishnan, P. M. Goldbart, and N. Mason, Approaching zero-temperature metallic states in mesoscopic superconductor–normal–superconductor arrays, *Nat. Phys.* **8**, 59 (2012).
- [36] G. Zhang, S. Turner, E. A. Ekimov, J. Vanacken, M. Timmermans, T. Samuely, V. A. Sidorov, S. M. Stishov, Y. Lu, B. Deloof, B. Goderis, G. V. Tendeloo, J. Van de Vondel, and V. V. Moshchalkov, Global and local superconductivity in boron-doped granular diamond, *Adv. Mater.* **26**, 2034 (2014).
- [37] V. V. Derevyanko, T. V. Sukhareva, and V. A. Finkel, Phase transitions and vortex structure evolution in two-level high-temperature granular superconductor $\text{YBa}_2\text{Cu}_3\text{O}_{7-\delta}$ under temperature and magnetic field, *Phys. Solid State* **59**, 1492 (2017).